Journal of Nanobiotechnology

RESEARCH Open Access

Engineered biomimetic cisplatin-polyphenol nanocomplex for chemo-immunotherapy of glioblastoma by inducing pyroptosis

Xinyan Hao[1,2], Yucheng Tang[1,2], Wenjie Xu[1,2], Ming Wang[4], Jiayi Liu[5], Yongjiang Li[6], Jun He[7], Yanjin Peng[1,2], Pengcheng Sun[1,2], Dehua Liao[8], Xiongbin Hu[1,2], Tiantian Tang[1,2], Min Zhou[1,2], Ruyue Han[1,2], Jiemin Wang[9], João Conde[10], Daxiong Xiang[1,2*] and Junyong Wu[1,2,3*]

Abstract

Glioblastoma multiforme (GBM) is characterized by pronounced immune escape and resistance to chemotherapy-induced apoptosis. Preliminary investigations revealed a marked overexpression of gasdermin E (GSDME) in GBM. Notably, cisplatin (CDDP) demonstrated a capacity of inducing pyroptosis by activating caspase-3 to cleave GSDME, coupled with the release of proinflammatory factors, indicating the potential as a viable approach of inducing anti-tumor immune activation. For the effective delivery of CDDP, the CDDP-polyphenol nanocomplexes were prepared, and catalase and copper ions were incorporated to fortify structural integrity, enhance glutathione (GSH) responsiveness, and ameliorate tumor hypoxia. Additionally, BV2 microglial cells were engineered to overexpress programmed death-1 (PD-1), and the membrane is employed for nanocomplex coating, effectively blocking the CDDP-induced upregulation of programmed death ligand 1 (PD-L1). Furthermore, the angiopep-2 peptide was modified to efficiently cross the blood brain barrier and specifically target GBM cells. In vitro analyses confirmed potent cytotoxicity and characteristic induction of pyroptosis. In vivo assays corroborated the enhancement of tumor targeting, culminating in an obvious suppression of tumor proliferation. A notable activation of immune cells was observed within tumors and lymph nodes, indicative of a synergistic effect of chemotherapy and immunotherapy, underscoring its potential as a safe and efficacious therapeutic strategy against GBM.

Keywords Glioblastoma, Pyroptosis, Cisplatin, Programmed death-1, Chemo-immunotherapy

*Correspondence:
Daxiong Xiang
xiangdaxiong@csu.edu.cn
Junyong Wu
wujunyong@csu.edu.cn
[1]Department of Pharmacy The Second Xiangya Hospital, Central South University, Changsha 410011, China
[2]Institute of Clinical Pharmacy, Central South University, Changsha 410011, China
[3]Hunan Key Laboratory of Tumor Models and Individualized Medicine, The Second Xiangya Hospital, Changsha, China
[4]Department of Neurosurgery The Second Xiangya Hospital, Central South University, Changsha 410011, China
[5]Department of Oncology, The Second Xiangya Hospital, Central South University, Changsha, Hunan 410011, China
[6]Center for Nanomedicine and Department of Anesthesiology, Brigham and Women's Hospital, Harvard Medical School, Boston, MA 02115, USA
[7]Department of General Surgery The Second Xiangya Hospital, Central South University, Changsha 410011, China
[8]Department of Pharmacy, School of Medicine, Hunan Cancer Hospital the Affiliated Cancer Hospital of Xiangya, Central South University, Changsha 410031, China
[9]Regenerative Medicine Institute, School of Medicine, University of Galway, Galway, Ireland
[10]ToxOmics, NOVA Medical School, Faculdade de Ciências Médicas, NMS|FCM, Universidade NOVA de Lisboa, Lisboa, Portugal

Introduction

Glioblastoma multiforme (GBM), the most malignant primary brain tumor, is typically treated with surgery, chemotherapy, or radiotherapy. Treatment efficacy remains limited owing to high recurrence rates and drug resistance, resulting in a 5-year survival rate of less than 6% [1, 2]. The potential of novel immunotherapy for GBM is compromised by the blood-brain barrier and immunosuppressive milieu [3]. Furthermore, chemotherapy-induced apoptotic GBM cells release RBM11-enriched extracellular vesicles, promoting proliferation and resistance to therapy [4]. Consequently, it is of paramount clinical significance to identify novel therapeutic strategies for traversing the blood brain barrier (BBB) and modifying GBM cell death modalities, thereby ameliorating the immunosuppressive microenvironment [5].

Pyroptosis is a form of programmed cell death mediated by gasdermin family proteins (GSDMA/B/C/D/E) and is characterized by cytoplasmic membrane pore formation and subsequent cell rupture [6, 7]. Pyroptosis is a pro-inflammatory process that releases substantial amounts of immunostimulatory factors, such as high mobility group protein B1 (HMGB1), and induces immune activation [8, 9]. The chemotherapeutic agent cisplatin (CDDP) activates caspase-3 to cleave GSDME, leading to the formation of GSDME-N-terminal structural domains that perforate the cellular membrane, thereby inducing pyroptosis [10]. However, most tumors lack GSDME expression due to hypermethylation of DFNA5 [11]. Notably, our preliminary research revealed higher GSDME expression in GBM, which also correlated with increased tumor malignancy and significantly reduced survival. Immunohistochemistry (IHC) confirmed abundant GSDME expression in tumor tissues of both GBM patients and GBM-bearing mice, suggesting GSDME as a potential therapeutic target for GBM (Fig. 1A-C).

We propose that CDDP induces pyroptosis via the caspase-3-GSDME pathway in GBM cells, with the subsequent release of immunostimulatory factors that potentially ameliorate the immunosuppressive microenvironment and enhance the immunological efficacy of chemotherapy. However, the application of CDDP is limited by its adverse effects and challenges of crossing the BBB [12]. Furthermore, abundant glutathione (GSH) in the tumor microenvironment can bind to CDDP, leading to diminished efficacy and drug resistance [13]. Therefore, ensuring adequate delivery of CDDP to GBM cells via efficient means might be pivotal in inducing pyroptosis.

Metal-polyphenol network nanostructures have emerged as a novel paradigm for sophisticated drug delivery systems [14–16]. The interaction between phenolic hydroxyl groups and Pt, along with the hydrophobicity of aromatic groups, facilitated the assembly of CDDP and polyphenol [17]. Additionally, we introduced Cu^{2+} into the system for further structural stabilization. Cu^{2+} can also deplete GSH abundant in the tumor microenvironment, effectively decreasing GSH and consequently enhancing the chemosensitivity of CDDP [18, 19]. Moreover, catalase (CAT) was integrated to improve the hypoxic microenvironment, further enhancing the antitumor efficacy [20, 21]. In addition, CDDP has demonstrated the capacity to further upregulate the immune checkpoint protein PD-L1 in tumor cells, and the synergistic application of CDDP and anti-PD-1 monotherapy markedly bolsters antitumor activity [22, 23]. Consequently, we encapsulated the system with membranes derived from engineered PD-1-overexpressed BV2 cells to increase the ability of BBB transversal and tumor targeting, block PD-L1 on the surface of GBM cells, revitalize $CD8^+$ effector T cell activity, and enhance immune efficacy.

Herein, we constructed a nanocomplex via the immediate assembly of CDDP, copper ions, tannic acid (TA) and catalase (CAT) using polyethylene glycol (PEG) as a nucleating agent. The nanocomposites were encapsulated in PD-1-BV2-derived membranes and modified with angiopep-2 peptides targeting the low-density lipoprotein receptor (LRP1), which is highly expressed on the membrane surface of brain microvascular endothelial cells and tumor cells, ensuring stable delivery and precise tumor accumulation [24]. The nanocomplex exhibited GSH/H_2O_2-responsive properties, and the released CDDP activated the caspase-3-GSDME pathway, leading to increased calreticulin (CRT) exposure and HMGB1 release, resulting in an anti-tumor immune response (Fig. 2). This study underscores the potential of CDDP delivery to provoke GBM cell pyroptosis, thereby amplifying the immunotherapeutic impact of chemotherapeutic interventions and offering a novel strategy for GBM immunotherapy.

Results and discussion

Synthesis and characterization

CDDP-incorporated nanocomposites (CuCCT) were synthesized via a catalase-facilitated assembly process. Dynamic light scattering (DLS) analysis indicated a uniform particle size distribution with a mean diameter of 83.52 nm, and exhibited good stability (Fig. 1D, Fig. S1). We further investigated the assembly mechanism of CuCCT using UV-vis spectroscopy. The UV-vis spectrum of CuCCT shifted significantly in NaCl and sodium dodecyl sulfate (SDS) solutions, indicating that electrostatic and hydrophobic interactions promoted the assembly process. In contrast, the UV-vis spectrum showed negligible change in urea solution, demonstrating that hydrogen bond interactions did not play a crucial role

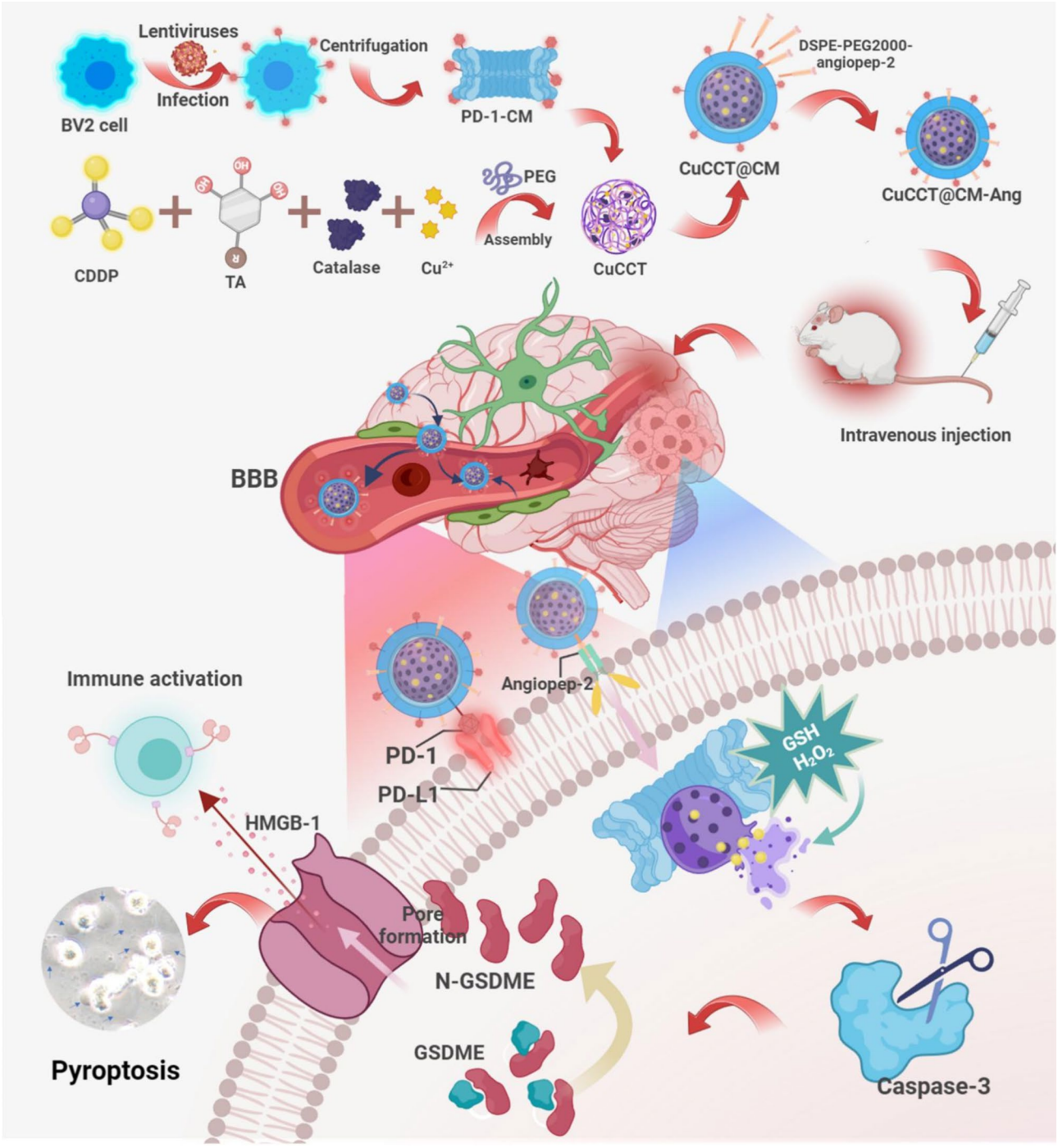

Fig. 1 Schematic illustration of the preparation of CuCCT@CM-Ang and the underlying mechanism of GBM treatment. Created with BioRender.com

(Fig. S2A-C). The size changes of CuCCT further confirmed the role of electrostatic and hydrophobic interactions in the assembly process (Fig. S2D). To augment the brain-targeting capabilities and immunomodulatory effects, BV2 microglial cell membranes were sonicated onto CuCCT (CuCCT@CM), increasing the particle size by approximately 31.88 nm (Fig. 1E). CuCCT and CuCCT@CM both exhibited good stability under serum conditions (Fig. S3). Subsequently, the angiopep-2 peptides were further modified on the cell membrane surface (CuCCT@CM-Ang) to enhance brain accumulation of the nanocomposites, exhibiting uniform particle size and commendable stability at 4℃ for two weeks (Fig. 1F, G, Fig. S4). CuCCT@CM-Ang exhibited a cumulative CDDP release of 61.25 ± 1.48% under serum conditions over 72 h (Fig. S5). Transmission electron microscopy

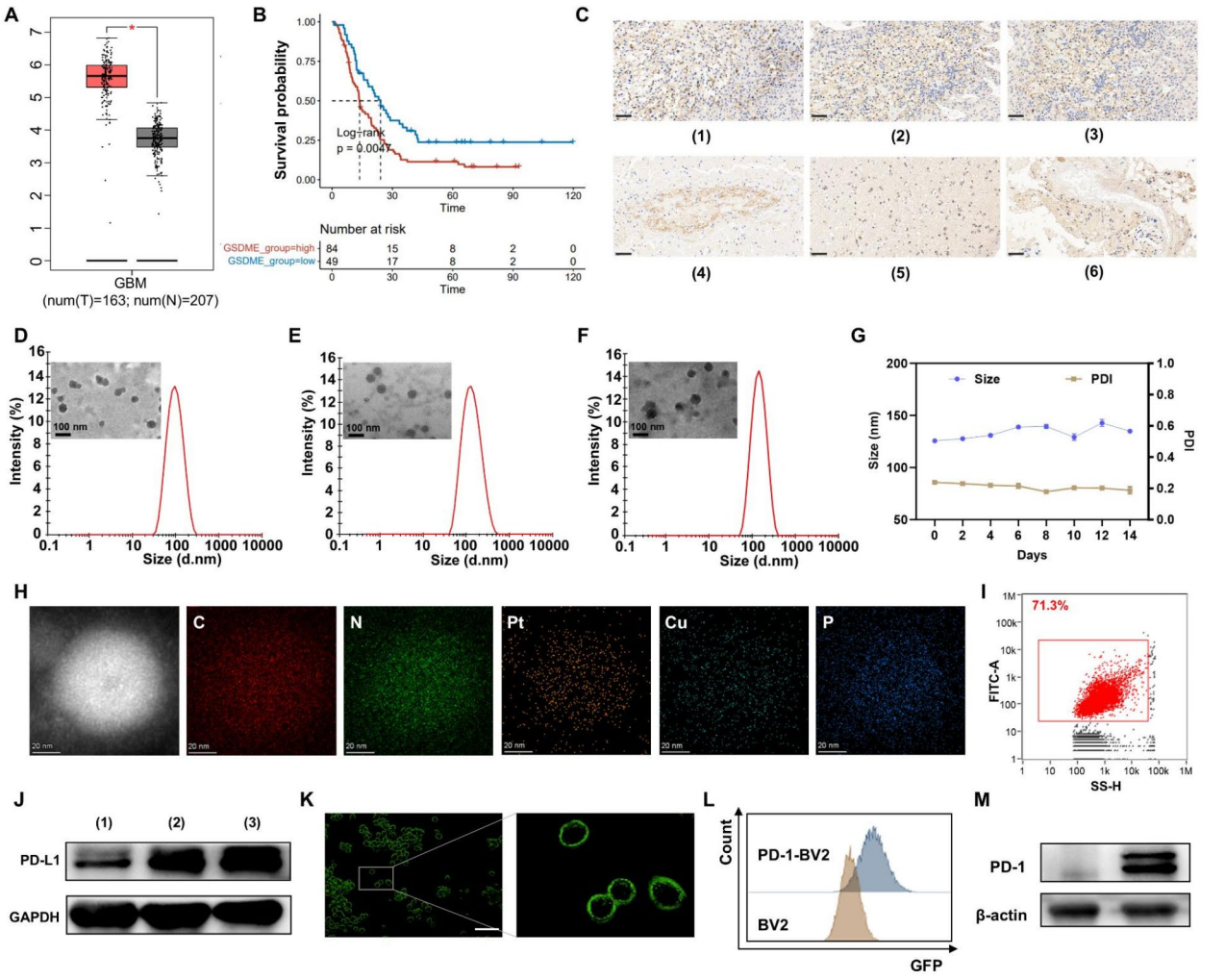

Fig. 2 The analysis of GSDME expression and characterization of nanocomposites. **A**) Differential expression of GSDME. **B**) Survival analysis of GBM patients with differentially expressed GSDME. **C**) IHC images of GSDME staining in GBM tissues from (1–3) tumor-bearing mice and (4–6) patients. Scale bar is 50 μm. Size distribution and TEM images of **D**) CuCCT, E) CuCCT@CM and F) CuCCT@CM-Ang. Scale bar is 100 nm. **G**) Stability of CuCCT@CM-Ang in 14 d. Results are presented as the mean ± SD ($n = 3$). **H**) HAADF-STEM and EDS mapping analysis of CuCCT@CM-Ang. Scale bar is 20 nm. **I**) Nanoflow cytometry analysis of the proportion of cell membrane-coated nanoparticles. **J**) PD-L1 expression in U87-MG cells after CDDP treatment. (1) Control, (2) 40 μM CDDP, and (3) 80 μM CDDP. **K**) Fluorescence images and **L**) FCM analysis of PD-1 expression. **M**) Expression of PD-1 in (1) BV2 cells and (2) engineered BV2 cells

(TEM) imaging confirmed the uniform distribution of the nanocomposites. Elemental mapping and energy-dispersive X-ray spectroscopy (EDS) confirmed the uniform distribution of Pt, Cu, and P within the nanocomposites, corroborating the successful integration of CDDP and an effective cell membrane coating (Fig. 1H, Fig. S6). The results of the nano-flow cytometry further demonstrated that the proportion of nanoparticles coated with the cell membrane was 71.3% (Fig. 1I). The loading efficiency for CDDP was approximately 9.12 ± 0.34%, and the encapsulation efficiency was 57.63 ± 2.15%.

GBM cells have been reported to exhibit expression of PD-L1 [25], and WB analysis revealed that treatment with CDDP further induced PD-L1 upregulation (Fig. 1J). Therefore, we engineered PD-1 overexpressed BV2 cells to extract membranes for nanocomposite coating, thereby blocking the PD-1/PD-L1 pathway. The PD-1 gene was encoded into a plasmid and transduced via lentivirus, and successful construction of PD-1-BV2 cells was visualized using green fluorescent protein (GFP) (Fig. 1K). Flow cytometry (FCM) results demonstrated a significant increase in PD-1 expression compared to native BV2 cells (Fig. 1L), and WB analysis corroborated the construction of PD-1 overexpressing cells (Fig. 1M). Moreover, Coomassie Brilliant Blue staining verified the integration of the membrane with the nanocomposites (Fig. S7).

Analysis of cellular uptake and GSH/H_2O_2 responsiveness

The uptake efficiency of the nanocomposites by U87-MG and GL261 cells was evaluated by confocal laser scanning microscopy (CLSM) and FCM analysis. CuCCT, CuCCT@CM, and CuCCT@CM-Ang exhibited increased fluorescence intensities, suggesting that cellular uptake was significantly enhanced by the construction of the nanocomplex and subsequent modifications, which was superior to that of free DiI and CuCCT. The intracellular fluorescence co-localized partially with the mitochondria, suggesting that the CDDP-loaded nanocomposites may induce pyroptosis through mitochondrial damage pathways (Fig. 3A). Moreover, quantitative FCM evaluation of fluorescence demonstrated a 3.7-fold increase in CuCCT@CM-Ang compared with free DiI, and a 1.5-fold increase compared with CuCCT group at 3 h post-treatment in U87-MG cells (Fig. 3B, C). Similar results were observed in GL261 and bEnd.3 cells, confirming the enhanced cellular internalization of CuCCT@CM-Ang (Fig. 3D-F, Fig. S8). Furthermore, we

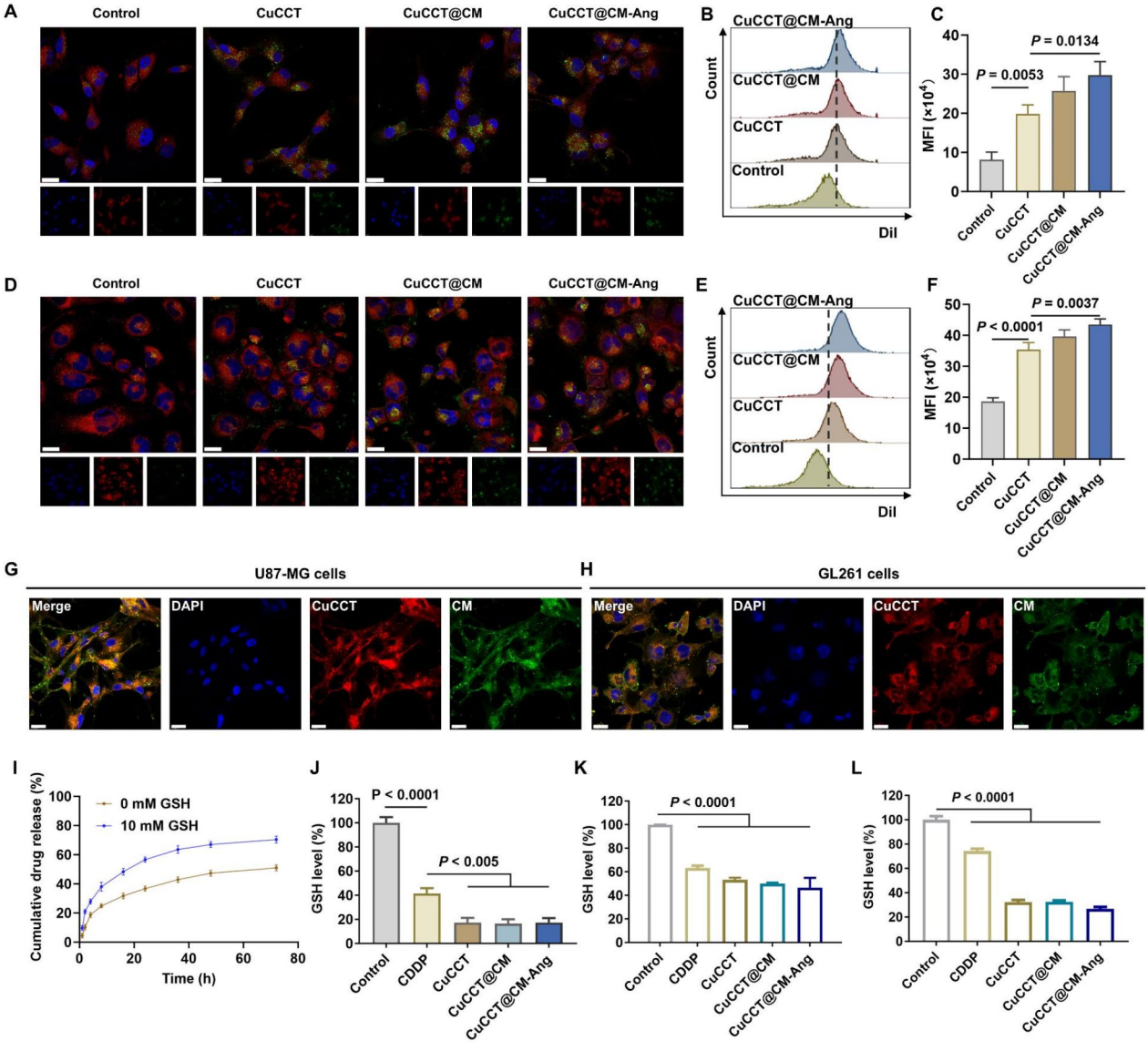

Fig. 3 Intracellular uptake and GSH responsiveness. **A**) Representative fluorescence images of U87-MG cells after incubation with CuCCT, CuCCT@CM, or CuCCT@CM-Ang for 3 h. Blue: DAPI stained nuclei; red: Mito-tracker; green: DiO. Scale bar = 20 μm. **B**) FCM analysis and **C**) quantification of fluorescence intensity in different groups. **D**) Representative fluorescence images, **E**) FCM analysis, and **F**) quantification of fluorescence intensity in GL261 cells. Scale bar = 20 μm. MFI, median fluorescence intensity. Intracellular co-localization of CuCCT and cell membrane (CM) in **G**) U87-MG and **H**) GL261 cells. Scale bar = 20 μm. **I**) Release profile of CDDP from CuCCT@CM-Ang in 0 and 10 mM GSH solutions. **J**) GSH concentration after incubation with CDDP, CuCCT, CuCCT@CM, or CuCCT@CM-Ang. Intracellular GSH levels in **K**) U87-MG and **L**) GL261 cells after treatment with CDDP, CuCCT, CuCCT@CM, or CuCCT@CM-Ang. Results are presented as mean ± SD ($n = 3$). *P* values were analyzed using one-way ANOVA

stained CuCCT and CM separately and then prepared CuCCT-CM-Ang. The CLSM images showed their co-localization within the cells, further demonstrating the effective coating of the nanocomposites with the cell membrane (Fig. 3G, H).

The nanocomposites decomposed in a tumor microenvironment rich in high concentrations of GSH and H_2O_2. The released copper ions and CAT further deplete GSH and promote the production of oxygen, which is crucial for enhancing the chemosensitivity of CDDP and improving the hypoxic environment. The release of CDDP from CuCCT@CM-Ang in the presence of GSH was monitored, and the findings revealed that 70.34 ± 2.33% of CDDP was discharged in a 10 mM GSH solution within 72 h, whereas only 50.94 ± 1.98% was released in phosphate-buffered saline (PBS) for the same duration (Fig. 3I). The capacity of the nanocomposites to deplete GSH was quantified, revealing that CuCCT@CM-Ang achieved an 82.64% reduction compared to the PBS group (Fig. 3J). The intracellular GSH levels post-treatment were also measured, with the CuCCT@CM-Ang group showing intracellular GSH levels of 46.59% and 26.60% relative to the PBS group in U87-MG and GL261 cells, respectively (Fig. 3K, L). These findings confirmed the GSH-responsive characteristics of the nanocomposites and their capability to diminish GSH levels, thereby amplifying the anti-tumor efficacy. The H_2O_2 responsiveness was also detected. A small amount of CuCCT could catalyze H_2O_2 to produce a high concentration of oxygen, indicating the strong catalytic capacity (Fig. S9). The generated oxygen potentially alleviates tumor hypoxia and consequently increases chemosensitivity.

In vitro antitumor efficacy evaluation

The cytotoxic effects of CDDP and the CDDP-loaded nanocomposites were quantitatively assessed in U87-MG and GL261 cells. CCK8 assay demonstrated a dose-dependent cytotoxic pattern for the nanocomposites. Compared to free CDDP, CuCCT, CuCCT@CM, and CuCCT@CM-Ang displayed superior antitumor capacities, potentially attributable to improved cellular internalization. The half-maximal inhibitory concentration (IC_{50}) values for CuCCT@CM-Ang were determined to 45.33 μM in U87-MG cells and 38.97 μM in GL261 cells (Fig. 4A, E). Correspondingly, fluorescent live/dead cell staining corroborated the augmented cytotoxicity of the CDDP-loaded nanocomposites (Fig. 4B, F). The rate of dead cells was further quantified by Annexin V-FITC/propidium iodide (PI) staining. The pores formed in the cell membrane induced by pyroptosis allow PI to enter the cytosol and bind to the nucleus, presenting the Annexin V^+ PI^+ feature. The mortality of U87-MG cells treated with CuCCT@CM-Ang was significantly elevated (50.70 ± 2.82%), surpassing that of free CDDP (31.08 ± 2.98%) and CuCCT (37.79 ± 3.04%) (Fig. 4C, D). A similar pattern was observed in GL261 cells, with a 49.47 ± 3.02% death rate after CuCCT@CM-Ang treatment, which was markedly higher than that induced by CDDP alone (32.27 ± 1.55%) (Fig. 4G, H). These findings collectively highlight the enhanced antitumor potency of the CDDP-loaded nanocomposites in vitro.

Exploration of pyroptosis dynamics

Pyroptosis is a pro-inflammatory variant of programmed cell death. Cellular rupture leads to subsequent exposure to CRT and the release of inflammatory cytokines, such as HMGB1, IL-1β, and IL-18, potentially stimulating anti-tumor immune responses and improving the tumor immunosuppressive microenvironment. We performed a comprehensive RNA-Seq analysis of PBS- and CuCCT@CM-Ang-treated U87-MG cells to elucidate the potential antitumor mechanisms (Fig. 5A). Gene set enrichment analysis (GSEA) results demonstrated the upregulation of EGFR tyrosine kinase inhibitor resistance, MAPK signaling pathway, and Rap1 signaling pathway (Fig. S10), indicating tumor inhibition. Moreover, comparative analysis showed that CuCCT@CM-Ang-treated cells highlighted the interferon alpha/gamma response and TNFα signaling via the NF-κB pathway (Fig. 5B), suggesting that CuCCT@CM-Ang-induced pyroptosis exhibited the potential to elicit immune activation.

We investigated the crucial characteristics associated with pyroptosis in GBM cells treated with CDDP and CDDP-loaded nanocomposites. During pyroptosis, cells swell until the cell membrane ruptures, leading to the release of cellular contents. The elevated release of lactate dehydrogenase (LDH) in the CuCCT@CM-Ang group confirmed its enhanced ability to induce pyroptosis (Fig. 5C, Fig. S11). Morphological images of post-treatment U87-MG and GL261 cells displayed typical swelling and vesicle formation (Fig. S12, S13). Scanning electronic microscopy (SEM) images also confirmed swelling and pore formation of the cells treated by CuCCT@CM-Ang, indicative of pyroptosis (Fig. 5D, E). Western blotting identified pyroptosis-specific proteins in treated cells exhibiting GSDME-N fragmentation and caspase-3 activation, indicating caspase-3-GSDME mediated pyroptosis. Notably, the exposure to CRT and the release of HMGB1 increased following CDDP and nanocomposite treatment compared to the control (Fig. 5F, G). A significant elevation of HMGB1 content was detected in the supernatant of cells treated with CDDP-loaded nanocomposites (Fig. 5H, Fig. S14). Furthermore, flow cytometry revealed a markedly higher proportion of CRT-positive cells (Fig. 5I, Fig. S15), consistent with the results of CLSM (Fig. 5J, Fig. S16). These augmented pro-inflammatory markers underscore the potential of CDDP-loaded nanocomposites to modulate the tumor

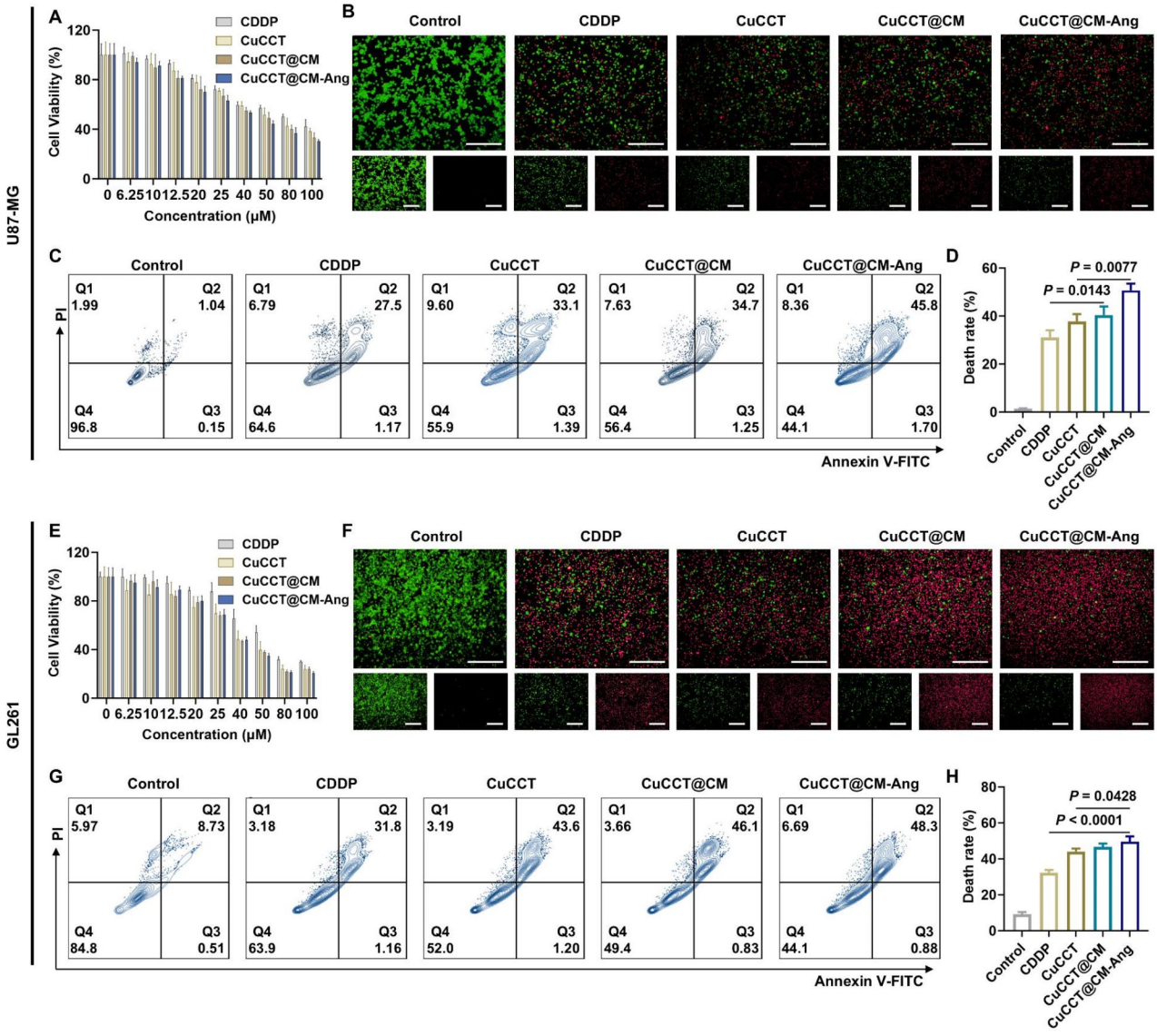

Fig. 4 Cytotoxicity investigation. **A**) CCK8 assay to examine cell viability in U87-MG cells after 24 h incubation with CDDP, CuCCT, CuCCT@CM, and CuCCT@CM-Ang. Concentration of CDDP was varied from 0 μM to 100 μM. **B**) Representative images of U87-MG cells via live/dead staining. **C**-**D**) FCM profile of proportion of cell death in U87-MG cells via Annexin V-FITC/PI staining assay. **E**) CCK8 assay, **F**) live/dead staining images, **G**-**H**) FCM assay of GL261 cells after treatment with different groups. Scale bar = 200 μm. Results are presented as mean ± SD ($n = 3$). *P* values were analysed by one-way ANOVA test

immune milieu, suggesting a strategy to potentiate antitumor immune activation.

Subsequently, we examined the modulatory effect of nanocomplex-induced pyroptosis on macrophage polarization. FCM analysis of BV2 cells indicated a pronounced polarization towards the M1 phenotype when incubated with tumor cells treated with CuCCT@CM-Ang (64.2 ± 4.34%) compared to the control group (43.1 ± 5.41%) (Fig. 5K, L). Furthermore, we evaluated the maturation of dendritic cells (DCs), a pivotal process in the initiation of immune responses following exposure to CDDP-induced pyroptosis. Bone marrow-derived dendritic cells (BMDCs) were cultured with U87-MG cells treated with the nanocomposites, leading to a significant elevation in the population of $CD80^+CD86^+$ BMDCs within the CuCCT@CM-Ang group (64.6 ± 5.35%) in comparison to the group co-cultured with untreated GBM cells (40.2 ± 5.19%) (Fig. 5M, N). A similar increase was observed in BMDCs incubated with post-treated GL261 cells (Fig. S17). These results collectively illuminated the capacity of CDDP-loaded nanocomposites to trigger immune activation, suggesting their potential to elicit strong antitumor effects.

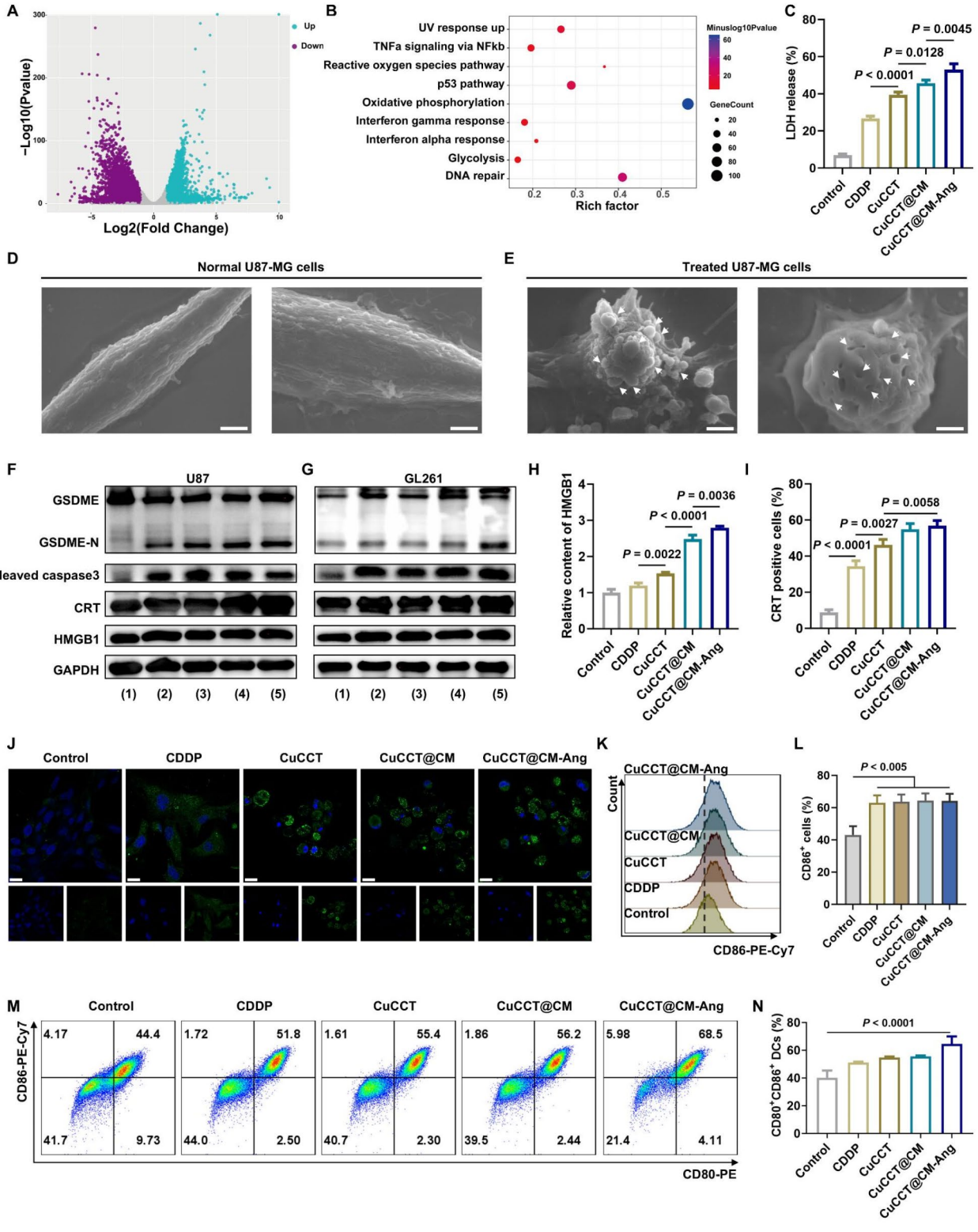

Fig. 5 (See legend on next page.)

(See figure on previous page.)

Fig. 5 Investigation of potential eliciting immune activation. **A**) Volcano plots of differentially expressed genes in U87-MG cells treated with CuCCT@CM-Ang. **B**) GSEA of signaling pathways upregulated in U87-MG cells treated with CuCCT@CM-Ang. **C**) LDH release in U87-MG cells after different treatments. Representative SEM images of **D**) normal U87-MG cells and **E**) CuCCT@CM-Ang-treated U87-MG cells. Arrows indicate plasma membrane bubbling and pore formation. WB analysis of GSDME-N fragmentation, caspase-3 activation, and expression of HMGB1 and CRT in (**F**) U87-MG and (**G**) GL261 cells after treatment with (1) PBS, (2) CDDP, (3) CuCCT, (4) CuCCT@CM, and (5) CuCCT@CM-Ang. **H**) Relative content of HMGB1 in the supernatant of U87-MG cells after different treatments. **I**) FCM analysis of CRT-positive cells after treatment. **J**) Representative images of immunofluorescence staining of CRT. Scale bar = 20 μm. **K**-**L**) Detection of macrophage polarization after incubation with U87-MG cells post-treatment with PBS, CDDP, CuCCT, CuCCT@CM and CuCCT@CM-Ang. **M**-**N**) Investigation of BMDC maturation after incubation with U87-MG cells post-treatment with PBS, CDDP, CuCCT, CuCCT@CM, and CuCCT@CM-Ang. Results are presented as mean ± SD ($n = 3$). *P* values were analysed by one-way ANOVA test

Investigation of BBB traversal ability and biodistribution

BBB penetration poses a great challenge for the efficient delivery of therapeutic agents to the tumor site. In our investigation, we employed an in vitro transwell model to evaluate the penetrative capacity of the nanocomposites across the BBB (Fig. 6A). We proceeded to introduce U87-MG/GL261 cells into the basal chamber, followed by an 8-hour incubation period with various treatments in the apical compartment, and images of nanocomposite translocation across the bEnd.3 cell monolayer were recorded using fluorescence microscopy. A marked augmentation in fluorescence within the basal compartment was observed in the CuCCT@CM and CuCCT@CM-Ang groups relative to that in the control group (Fig. 6B, Fig. S18). This enhancement suggests that biomimetic modifications involving membrane coating and further incorporation of targeted peptides substantially contribute to the ability to traverse the BBB with greater efficiency.

Subsequently, the in vivo targeting efficacy of CuCCT@CM-Ang was investigated through intravenous administration of DiR and DiR-labeled nanocomposites into GL261 murine models. Imaging via the IVIS system at intervals of 8, 24, and 48 h post-injection revealed that the membrane coating markedly augmented the precision of targeting to the tumor sites, outperforming both the CuCCT and free DiR groups. Tumor accumulation was further amplified by incorporation of the angiopep-2 peptide. Notably, the CuCCT@CM-Ang group exhibited a progressive increase in fluorescence signals within the brain, which peaked at 24 h, followed by a decrease at 48 h (Fig. 6C, D, E). Comparative analysis at multiple time points indicated substantially heightened fluorescence within the tumors of both the CuCCT@CM and CuCCT@CM-Ang groups. Ex vivo imaging at 24 h indicated accumulation within primary organs, notably the liver, spleen, and lungs, with the CuCCT@CM-Ang group exhibiting significant brain fluorescence (Fig. 6F, G). In a further corroboration of the tumor targeting capacity, DiO and DiO loaded nanocomposites were administered to the tumor bearing mice and the DiO accumulation at 24 h was assessed. The results revealed markedly elevated green fluorescence within the tumor of the CuCCT@CM-Ang group relative to other groups, thereby substantiating the enhanced GBM-targeting ability (Fig. 6H). Further in vivo pharmacokinetic studies revealed that CuCCT@CM-Ang exhibited a significantly prolonged blood retention time compared to free CDDP, indicating that the functionalized biomimetic nanocomplexes are better at evading systemic clearance. Additionally, CuCCT@CM-Ang showed markedly enhanced accumulation in the tumor tissues at 24 h, demonstrating its improved targeting capability (Fig. S19).

Therapeutic efficacy and immune activation

The in vivo therapeutic effect was investigated using a GL261-luc GBM murine model. Tumor-bearing mice were divided into six distinct groups: PBS, CDDP, CuCCT, CuCCT@CM, and CuCCT@CM-Ang, with temozolomide (TMZ) serving as a comparative control. The administration regimen is shown in Fig. 7A, and the progression of GL261-luc glioblastoma was monitored via bioluminescence imaging using the IVIS system. Compared to the other treatment groups, CuCCT@CM exhibited superior tumor suppression, as indicated by weaker bioluminescence, whereas CuCCT@CM-Ang exhibited enhanced outcomes attributable to augmented biotargeting capabilities (Fig. 7B, C). Terminal magnetic resonance imaging (MRI) of tumor volumes post-treatment revealed that the CuCCT@CM-Ang group exhibited the most significant inhibition in tumor size, corroborating the bioluminescent quantification observed during treatment (Fig. 7D, E). Throughout the observation period, the results revealed sequential mortality within the PBS, CDDP, CuCCT, and TMZ groups, whereas the CuCCT@CM and CuCCT@CM-Ang groups exhibited no fatalities and significantly extended survival (Fig. 7F). The results substantiated that CuCCT@CM and CuCCT@CM-Ang treatments resulted in the most pronounced tumor suppression, as evidenced by the minimal tumor area within the brain relative to other groups via hematoxylin-eosin staining (H&E) staining. IHC analysis of Ki67 staining was performed to quantify the antiproliferative effect on GBM. Ki67-positive cellular populations were notably abundant in the PBS group and markedly reduced in the CuCCT@CM and CuCCT@CM-Ang groups, underscoring their potent anti-proliferative properties. Moreover, HIF-1α staining indicated an obvious improvement in the hypoxic environment of the CuCCT@CM-Ang group (Fig. 7G).

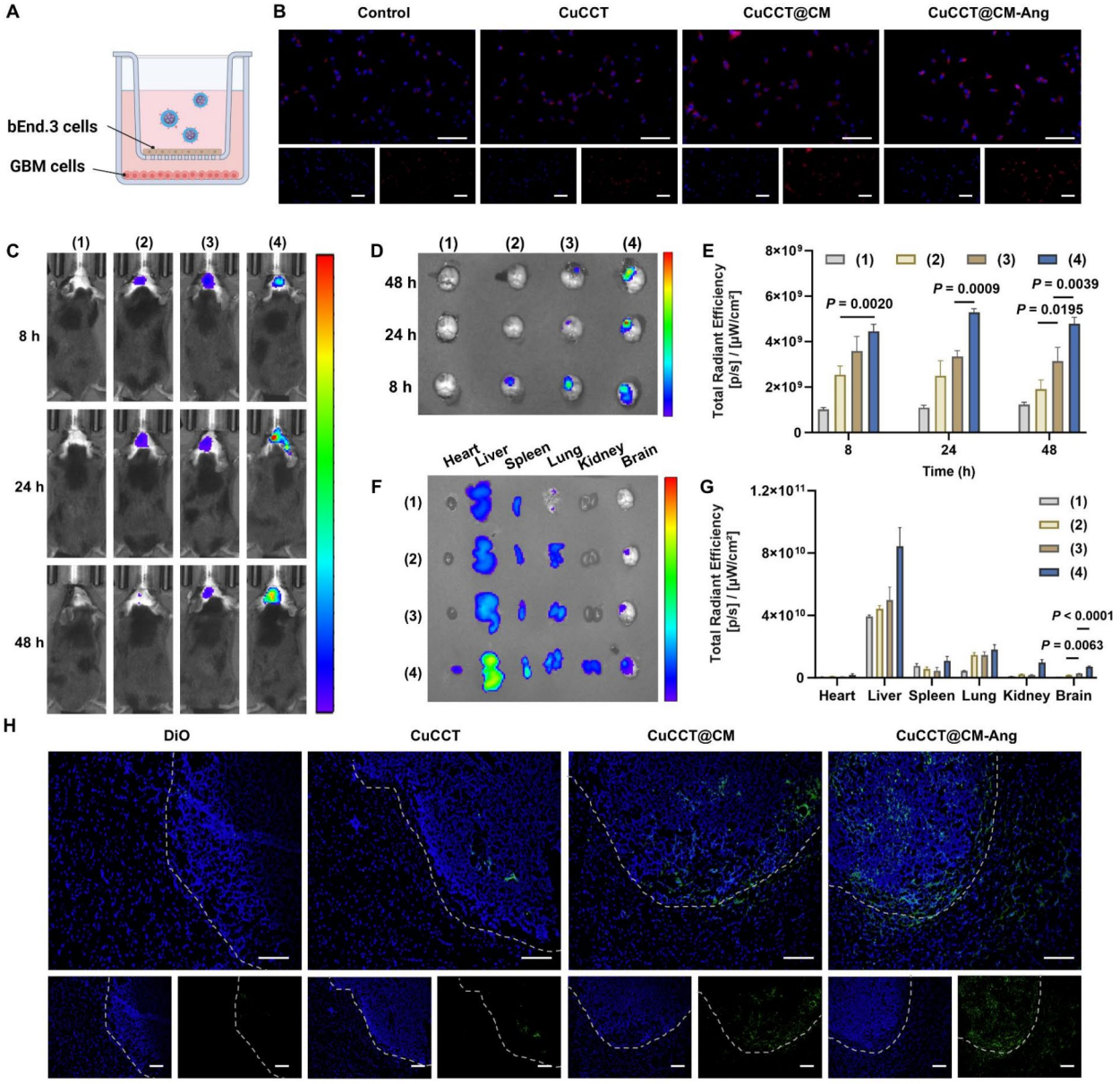

Fig. 6 Investigation of tumor-targeting capacity. **A**) Schematic diagram of the in vitro BBB model. **B**) Fluorescence images of the U87-MG cells in the lower chamber after incubation for 8 h. Blue: nuclei stained with DAPI; red: DiI. Scale bar = 50 μm. **C**) In vivo fluorescence imaging in GL261 models after injection of (1) DiR, (2) CuCCT, (3) CuCCT@CM, and (4) CuCCT@CM-Ang at 8, 24, and 48 h. **D**-**G**) IVIS imaging and quantification of fluorescence in tumors and major organs in vitro. **H**) Fluorescence images of brain tissue after injection of (1) DiO, (2) CuCCT, (3) CuCCT@CM, and (4) CuCCT@CM-Ang. Blue: cell nuclei stained with DAPI; green: DiO. Scale bar = 100 μm. Results are presented as mean ± SD ($n = 3$). *P* values were analysed by one-way ANOVA test

Terminal histopathological examination via H&E staining of the major organs (heart, liver, spleen, lung, and kidney) revealed no discernible toxicity. Biochemical assays of hepatic and renal parameters within the circulatory system indicated levels within standard ranges, thereby validating the biocompatibility of CuCCT@CM and CuCCT@CM-Ang (Fig. S20).

The ensuing investigation investigated the immune response elicited by CDDP-induced pyroptosis. Initial assays in tumor tissues indicated an increase in classical pyroptotic cytokines (IL-1β and IL-18) in mice administered CuCCT@CM-Ang, demonstrating a pivotal role in mitigating the tumor immunosuppressive microenvironment. Furthermore, the CuCCT@CM-Ang group also exhibited augmented levels of tumor necrosis factor (TNF-α) and interferon-γ (IFN-γ), signifying activation of cytotoxic T lymphocytes (Fig. S21). Subsequently, we quantitatively assessed the proportion of various immune

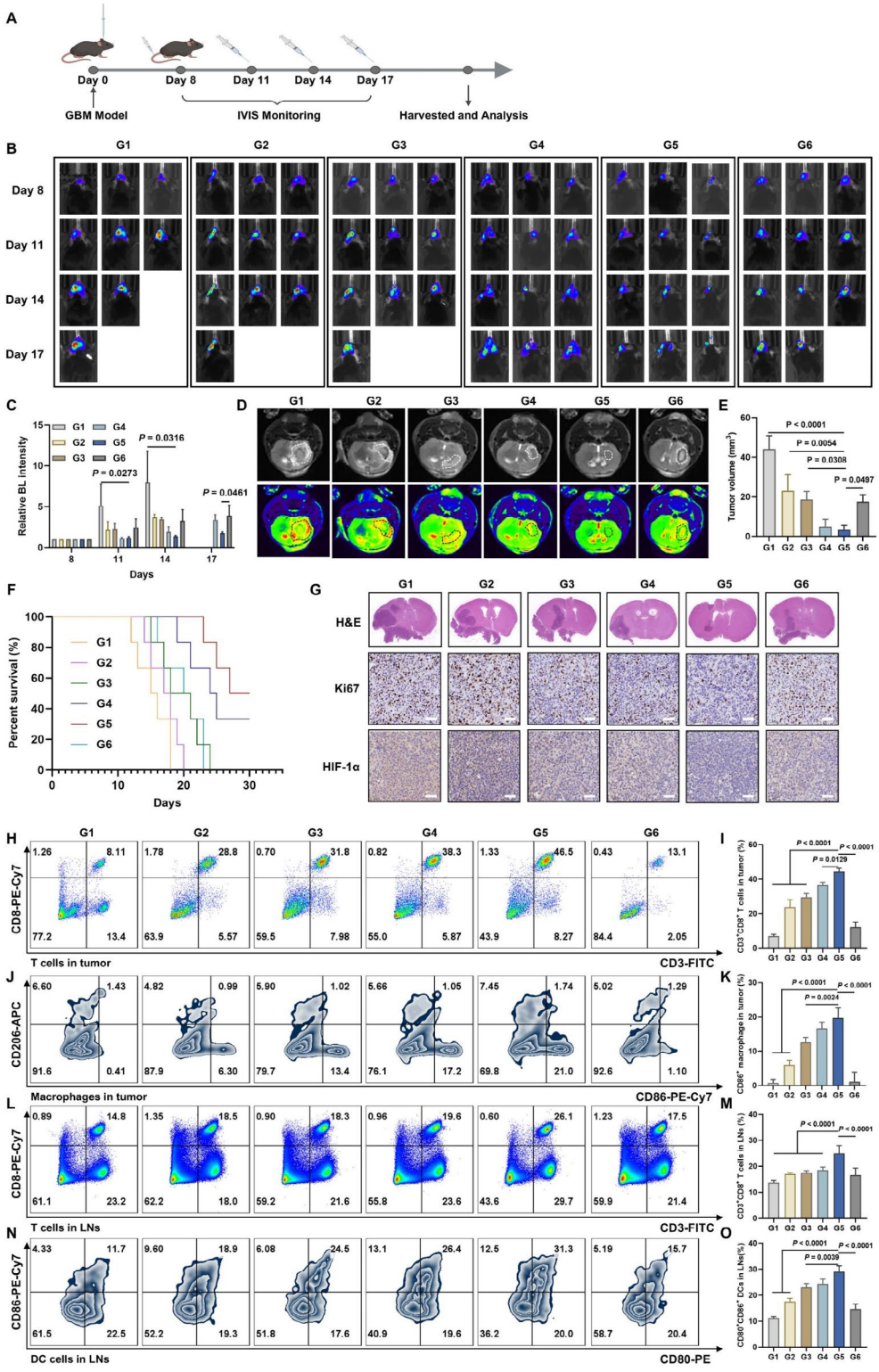

Fig. 7 Therapeutic efficacy in GL261-bearing mice. **A**) Schematic representation of the treatment schedule. **B**) Bioluminescence images and **C**) quantitative analysis of tumor-bearing mice on days 8, 11, 14, and 17. PBS (G1), CDDP (G2), CuCCT (G3), CuCCT@CM (G4), CuCCT@CM-Ang (G5), and TMZ (G6). **D**) Terminal MRI images and **E**) tumor volumes of the different groups after treatment. **F**) Survival curve ($n = 6$). **G**) H&E, Ki67, and HIF1α staining of tumor tissues. Scale bar = 50 μm. **H**-**I**) Proportion of $CD3^+CD8^+$ T cells in the tumor. **J**-**K**) Proportion of $CD86^+$ macrophage in tumor. **L**-**M**) Proportion of $CD3^+CD8^+$ T cells in the lymph nodes. **N**-**O**) Proportion of $CD80^+CD86^+$ DC cells in lymph nodes. *P* values were analysed by one-way ANOVA test

cells in the tumors and lymph nodes after treatment (Fig. S22-24). Remarkably, the infiltration of $CD8^+$ T lymphocytes intensified in mice subjected to CDDP and nanocomposite treatment, with the CuCCT@CM-Ang group exhibiting a substantial increase from 6.97 ± 1.05% to 44.47 ± 1.88% (Fig. 7H, I). Flow cytometry data also revealed a significant elevation in the subset of $CD11b^+$ $F4/80^+$ $CD86^+$ macrophages in the tumors, escalating an increase to 19.77 ± 2.95% compared to the CDDP group (5.85 ± 1.50%), indicative of augmented immune activation and potent antitumor immunity (Fig. 7J, K). Additionally, the proportions of activated DCs and $CD8^+$ T lymphocytes in the deep cervical lymph nodes were significantly increased. The CuCCT@CM-Ang group demonstrated an increase in the proportion of $CD8^+$ T lymphocytes (24.93 ± 2.97%) and DCs (29.07 ± 2.25%) compared to the control group, thereby underscoring the potential to induce immune activation within the lymph nodes (Fig. 7L-O). Collectively, these results indicate the capability of CuCCT@CM-Ang to elicit an effective antitumor response via lymph node amplification.

Materials and methods

Materials

CDDP was purchased from MedChemExpress LLC (Shanghai, China). Polyethylene glycol monomethyl ether 10,000 (PEG10000), copper chloride dihydrate ($CuCl_2{\cdot}2H_2O$), catalase (CAT), and tannic acid (TA) were purchased from Sigma-Aldrich (USA). 2-(4-amidinophenyl)-1 H-indole-6-carboxamidine (DAPI), 3,3′-dioctadecyloxacarbocyanine perchlorate (DiO), 1,1-dioctadecyl-3,3,3',3'-tetramethylindocarbocyanine perchlorate (DiI), 1,1-dioctadecyl-3,3,3,3-tetramethylindotricarbocyaine iodide (DiR) were purchased from Yeasen (Shanghai, China). Cell culture plates, dishes, and tubes were purchased from NEST Biotechnology (Wuxi, China). Dulbecco's Modified Eagle's Minimum Essential Medium (DMEM) was purchased from Pricella (Wuhan, China). Fetal bovine serum (FBS) were purchased from ExCell Bio (Jiangsu, China). Penicillin-Streptomycin solution, 0.25% trypsin ethylene diamine tetraacetic acid (EDTA) and Cell Counting Kit-8 (CCK8) were purchased from NCM Biotech (Suzhou, China). Mito-Tracker Red CMXRos was purchased from Beyotime (Shanghai, China). Reduced GSH Content Assay Kit (BC1175) was purchased from SolarBio (Beijing, China). Annexin V-FITC/Propidium iodide (PI) Cell Apoptosis Kit and BCA Protein Assay Kit were purchased from Beyotime Biotechnology (Shanghai, China). IL-1β, IFN-γ and TNF-α ELISA kit were purchased from BioLegend, Inc. (CA, USA). IL-18 ELISA kit was purchased from Thermo Fisher Scientific Inc. (MA, USA). HMGB1 ELISA kit (JONLNBIO, JL13702) was purchased from Jianglai biology (Shanghai, China). Antibodies for flow cytometry were purchased from BD Biosciences (New Jersey, USA), including fixable viability dye efluor 506, anti-CD16/CD32, anti-CD45-APC-eflour78, anti-CD3e-FITC, anti-CD4-APC, anti-MHCII-PerCP-eFlour710, anti-CD8-PE-Cy7, anti-CD11c-APC, anti-CD80-PE, anti-CD86-PE-Cy7, and anti-CD206-APC. HMGB1 Rabbit mAb (P17030) was purchased from ProMab Biotechnologies Inc. (Changsha, China). PD-L1 rabbit mAb, CRT Rabbit pAb, GAPDH Rabbit pAb, and β-actin rabbit pAb, were purchased from Abclonal (Wuhan, China).

Cell lines and animals

BV2 microglial cells, U87-MG human glioma cells, and GL261 murine glioma cells were purchased from the National Collection of Authenticated Cell Cultures and cultured in DMEM with 10% FBS and 1% penicillin-streptomycin at 37℃ with 5% CO_2. Male C57BL/6 mice (7 weeks old) were obtained from the SJA Laboratory Animal Co., LTD (Changsha, China). The animals were raised in SPF environment.

Establishment and characterization of PD-1-BV2 cell lines

Murine PD-1 lentiviral transfer plasmids and lentivirus packaging plasmids were purchased from Youbio. The lentivirus was produced in 293T cells by co-incubation with PD-1 overexpression transfer plasmids, accessory vectors and transfection reagent. The supernatant was harvested after 72 h and concentrated by centrifugation. Next, the lentiviruses were added to the BV2 cells for infection, and after 24 h, the cells were cultured in fresh culture medium with 5 μg/mL puromycin to screen the engineered stable PD-1-BV2 cells with higher purity. The cells were observed by fluorescence microscopy to determine GFP expression, and single-cell suspensions of PD-1-BV2 and BV2 cells were collected and detected by flow cytometry.

Extraction of PD-1-BV2 cell membrane

PD-1-BV2 cell membrane was extracted by density gradient centrifugation. The cells were resuspended in ice-cold isolation buffer (Tris-HCl solution with 200 mM mannitol and 76 mM sucrose; pH 7.4). Bovine serum albumin (5 mg/ml), EDTA-Na_2 (1.5 mM), and a protease phosphatase inhibitor cocktail were sequentially added to prevent protein degradation. The cells were then lysed using an ultrasonic cell disrupter (100 W, 20 s on/30 s off, 14 min) and centrifuged at 800 g and 10,000 g for 10 min. Finally, PD-1-BV2 cell membranes were collected by ultracentrifugation at 100,000 × g for 60 min, and protein content was measured using a BCA protein assay kit. The cell membrane was stored at -80℃ for further use.

Preparation and characterization of CDDP-based nanocomposites

Cisplatin was dissolved in deionized water, and 200 μl PEG 10,000 (20 mg/ml), 200 μl catalase (10 mg/ml), 96 μl copper chloride dihydrate (5 mg/ml), and 200 μl tannic acid (5 mg/ml) were added dropwise to the cisplatin solution and stirred for 20 min. The mixture was centrifuged at 10,000 rpm for 20 min to remove unassembled components and then resuspended to obtain the CuCCT. Subsequently, CuCCT@CM (membrane-coated CuCCT) was prepared using an ultrasonic method. CuCCT and PD-1-BV2 cell membranes were mixed at a mass ratio of 4:1, and ultrasound was performed for 2 min. DSPE-PEG2000-Angiopep-2 (TFFYGGSRGKRNNFKTEEY, Ruixi Biological Technology Co.,Ltd. Xi'an, China) was co-incubated with CuCCT@CM at 37℃ for 15 min to develop CuCCT@CM-Ang. The size distribution and zeta potentials of CuCCT, CuCCT@CM, and CuCCT@CM-Ang were analyzed using a Zetasizer (ZS90, Malvern, UK). The size distribution of CuCCT@CM-Ang was assessed using nanoparticle tracking analysis (NTA, Nanosight NS300, Malvern, UK). The morphology and elemental distribution of the nanoparticles were observed using transmission electron microscopy (TEM) and energy dispersive spectrometry (EDS) (Titan G2 60–300, FEI Company, Oregon, USA). The nanocomposites were stored at 4℃, and the size distribution and PDI were recorded every two days over a 14-day period to assess the storage stability. Additionally, the nanocomposites were mixed with a 10% serum solution, the size variations were measured at different time points to evaluate their stability in serum.

The concentration of CDDP was detected by inductively coupled plasma optical emission spectrometer (ICP-OES, Spectro Blue, Kleve, German), and the encapsulation efficiency (EE) and loading efficiency (LE) were further calculated: EE (%) = (mass of loaded CDDP / mass of initial CDDP) × 100%; LE (%) = (mass of loaded CDDP / mass of nanocomposites) × 100%.

Cellular uptake

The cellular uptake efficiency was determined using confocal laser scanning microscopy (CLSM) and flow cytometry (FCM, Cytek NL3000, Cytek Biosciences, China). The U87-MG/GL261/bEnd.3 cells were seeded in 24-well plates (5×10^4 cells per well) and cultured overnight. Free DiI and nanocomposites loaded with DiI were incubated with cells for 3 h, and the cells were washed with PBS for twice. Cell nuclei were stained with DAPI for 10 min, and the images were observed using CLSM.

GSH depletion

GSH depletion abilities of the formulations were also assessed. GSH (25 mM) was mixed with CDDP, CuCCT, CuCCT@CM, or CuCCT@CM-Ang. After 30 min, GSH levels were measured using a GSH content kit. Intracellular GSH levels were then evaluated. GL261/U87-MG cells were seeded in 6 well plates (1×10^5 cells per well) and cultured overnight. Cells were incubated with CDDP, CuCCT, CuCCT@CM, or CuCCT@CM-Ang for 20 h. After treatment, the cells were harvested and lysed, and intracellular GSH levels were measured. The release kinetics of CDDP under different GSH conditions were assessed by mixing CuCCT with GSH solutions (0 and 10 mM). Samples were collected at different time points, and the concentrations were measured.

Cytotoxicity

The cytotoxicity of CDDP, CuCCT, CuCCT@CM, and CuCCT@CM-Ang was measured using the CCK8 assay. Briefly, U87-MG/GL261 cells were seeded in a 96-well plate (4×10^3 cells/well) and cultured overnight. After treatment with CDDP and CDDP-loaded nanocomplexes at a series of concentration (0-100 nM) for 24 h, the supernatant was removed and 100 μl CCK8 solution was added and incubated for 1 h. Absorbance was measured at a wavelength of 450 nm. A live/dead assay was also performed on U87-MG/GL261 cells after different treatments. The cells were seeded into 12-well plates (2×10^5 cells/well) and cultured overnight. After incubation with CDDP and CDDP-loaded nanocomplexes, the cells were stained with calcein-AM and PI and imaged using a fluorescence microscope. The percentage of cell death was quantified using an Annexin V-FITC/PI staining assay. Briefly, 2×10^5 U87-MG/GL261 cells were seeded into 12-well plates. The cells were stained with Annexin V-FITC and PI after different treatments and analyzed by FCM.

Investigation of pyroptosis characteristics

U87-MG/GL261 cells were seeded into 6-well plates (1×10^6 cells/well), and pyroptosis morphology was observed by microscopy after treatment with CuCCT@CM-Ang for 48 h. The cells were collected and lysed, and pyroptosis biomarkers (GSDME, GSDME-N caspase-3, and cleaved caspase-3) were detected by western blotting. The CRT and HMGB-1 expression levels were also assessed. Lactate dehydrogenase (LDH) levels in the supernatant were detected using an LDH assay kit.

The HMGB1 content in the supernatant of the treated cells was detected using the ELISA method according to the instructions. The cells were collected, incubated with anti-CRT antibody and analyzed by FCM. Additionally, the immunofluorescence method was used to further evaluate CRT exposure. The treated cells were fixed with 4% formaldehyde and blocked with 5% BSA solution for 20 min. The cells were incubated overnight at 4 °C with anti-CRT antibodies, followed by a 1-hour incubation

with Alexa Fluor 488-conjugated secondary antibodies at room temperature in the dark. The nuclei were stained with DAPI. Fluorescence images were captured using CLSM.

Immune cells activation

BMDCs were extracted from 6-week-old male C57BL/6 mice. Cells from the bone marrow were cultured in 1640 medium with GM-CSF (20 ng/ml) and 2-mercaptoethanol (50 μM) for 7 days. U87-MG/GL261 cells were seeded into 24-well plates (1×10^6 cells/well) and incubated with CDDP, CuCCT, CuCCT@CM, and CuCCT@CM-Ang for 40 h. The supernatant was removed and BMDCs/BV2 cells were added into each well. After co-incubation for 24 h, the BMDCs were stained with anti-PE-CD80 and anti-APC-CD86. BV2 cells were stained with anti-APC-CD86. The cells were detected by FCM.

In vivo biodistribution and tumor targeting

An orthotopic GBM model was established, as previously described [26]. Mice were anesthetized, and 10 μl GL261-luc cells (2×10^6 cells) were implanted into the left striatum using a microsyringe pump. Biodistribution and tumor-targeting efficacy were examined 10 days post-implantation, with free DiR or DiR-loaded nanoparticles administered intravenously to tumor-bearing mice. Fluorescence distribution was monitored by IVIS imaging at various time points post-injection (8, 24, and 48 h), and ex vivo fluorescence signals were examined in excised major organs.

Therapeutic efficacy and immune mechanism exploration

Therapeutic efficacy was evaluated using a GL261 model. Mice were randomly divided into six groups and subjected to intravenous injections of PBS, CDDP, CuCCT, CuCCT@CM, or CuCCT@CM-Ang (5 mg/kg CDDP) every three days for a total of four doses. The tumor dimensions and body weights were monitored. Mice were euthanized at the experimental endpoint, brains were harvested for H&E and IHC analyses, and major organs were subjected to H&E staining for systemic toxicity assessments.

Tumors and lymph nodes were harvested to identify immune activation. Cells were incubated with the fixable viability dye efluor 506 to discern live/dead cells. T cells were labeled with antibodies against CD45, CD3, and CD8. Macrophages were characterized using antibodies against CD45, CD11b, F4/80, CD206, and CD86. Dendritic cells were stained with antibodies against CD45, CD3, CD11c, MHCII, CD80, and CD86. FCM was used to analyze the cell populations.

Statistical analysis

Statistical analyses were conducted using the GraphPad Prism software (version 10.0). Data are presented as mean ± standard deviation (SD), and multiple comparisons were performed using one-way analysis of variance (ANOVA).

Conclusion

GBM presents a formidable challenge owing to its propensity for immune evasion and chemotherapeutic resistance, underscoring the urgent need for efficacious treatment approaches. Recent advancements in nanotherapeutic strategies based on pyroptosis are continually evolving. Various nanoplatforms and novel combination therapies using small molecule drugs, protein drugs, or nucleic acid drugs have been developed to induce tumor cell pyroptosis and reshape the tumor immune microenvironment. Additionally, selectively increasing the levels of GSDM protein in tumor cells is currently one of the main focuses of research to induce cell pyroptosis. Our preliminary investigation demonstrated elevated GSDME expression in GBM tumors, suggesting the induction of pyroptosis mediated by the caspase-3-GSDME pathway as a novel therapeutic method for GBM treatment. Based on this, we constructed a biomimetic nanocomposite to facilitate the targeted delivery and BBB penetration of CDDP, thereby inducing pyroptosis in GBM cells and promoting immune activation. CDDP, copper ions, CAT, and TA formed a nanocomposite that possessed GSH/H_2O_2 responsiveness, synergistically enhancing chemosensitivity and therapeutic efficacy. Moreover, GBM cells expressed PD-L1 and our preliminary study confirmed that CDDP treatment further upregulated PD-L1 expression. Therefore, we engineered PD-1-overexpressed BV2 cells to extract cell membranes for nanocomposite modification, thereby enhancing the homologous targeting and blocking of the PD-1/PD-L1 pathway. The nanocomplexes significantly enhanced cellular internalization and cytotoxicity in GBM cells. The induction of pyroptosis in tumor cells was accompanied by CRT exposure and the release of HMGB1, intimating its potential role in synergistically provoking tumor-specific immune responses. The in vivo analyses corroborated the ability of the CuCCT@CM-Ang nanocomposite to precisely target the tumor sites and elicit robust antitumor activity in GBM models, suggesting a promising therapeutic strategy for the management of GBM.

Abbreviations

GBM	Glioblastoma multiforme
GSDME	Gasdermin E
CDDP	Cisplatin
GSH	Glutathione
PD	1-Programmed death-1
PD	L1-Programmed death ligand 1
HMGB1	High mobility group protein B1

BBB	Blood brain barrier
IHC	Immunohistochemistry
CAT	Catalase
TA	Tannic acid
PEG	Polyethylene glycol
LRP1	Low-density lipoprotein receptor
CRT	Calreticulin
CuCCT	CDDP-incorporated nanocomposites
CuCCT@CM	Cell membrane-coated CuCCT
CuCCT@CM	Ang-Angiopep-2 peptide-modified CuCCT@CM
DLS	Dynamic light scattering
SDS	Sodium dodecyl sulfate
TEM	Transmission electron microscopy
EDS	Elemental mapping and energy-dispersive X-ray spectroscopy
FCM	Flow cytometry
LDH	Lactate dehydrogenase
SEM	Scanning electronic microscopy
DCs	Dendritic cells
BMDCs	Bone marrow-derived dendritic cells
TNF	α-Tumor necrosis factor
IFN	γ-Interferon-γ
DAPI	2-(4-amidinophenyl)-1 H-indole-6-carboxamidine
DiO	3,3′-dioctadecyloxacarbocyanine perchlorate
DiI	1,1-dioctadecyl-3,3,3′,3′-tetramethylindocarbocyanine perchlorate
DiR	1,1-dioctadecyl-3,3,3,3-tetramethylindotricarbocyaine iodide

Supplementary Information

The online version contains supplementary material available at https://doi.org/10.1186/s12951-025-03091-w.

Supplementary Material 1

Author contributions

JW and DX: supervision. JW and XH and YT: conceptualization, methodology, software, experiment, data curation, wrote-origin draft, and editing. MW, YL, JH and WX: part of the experiments and original draft writing. JL: formal analysis and data curation. YP, PS and DL: conceptualization and writing revision. XH, TT, MZ and RH, JW and JC: review & editing.

Funding

This research was supported by National Natural Science Foundation of China (Grant No. 82373295, No. 82304424), Natural Science Foundation of Hunan Province (Grant No. 2023JJ60505, No. 2023JJ40860, No.2024JJ4081, No.2024JJ5480), The Science and Technology Innovation Program of Hunan Province (No. 2024RC3061), Natural Science Foundation of Changsha, Hunan Province, China (Grant No. kq2208346), China Postdoctoral Science Foundation (Grant No. 2023M733962), Postdoctoral Fellowship Program of CPSF (Grant No.GZB20230873), Health Commission of Hunan province, China (No.W20242009, No.W20243128). J.C. acknowledges the European Research Council (ERC) under the European Union's Horizon 2020 Research and Innovation Program (ERC-StG-2019-848325).

Data availability

No datasets were generated or analysed during the current study.

Declarations

Ethics approval and consent to participate

All animal experiments were performed according to the protocols and reviewed and approved by the Institutional Animal Care and Use Committee (IACUC) of the Second Xiangya Hospital, Central South University, China (20220623).

Competing interests

J.C. is a co-founder and shareholder of TargTex S.A. – Targeted therapeutics for Glioblastoma Multiforme. J.C. is also a member of the Global Burden Disease (GBD) consortium of the Institute for Health Metrics and Evaluation (IHME), University of Washington (US) and is in the Scientific Advisory board of Vector Bioscience Cambridge. The other authors declare no conflict of interest.

Received: 5 September 2024 / Accepted: 2 January 2025
Published online: 15 January 2025

References

1. Ostrom QT, Gittleman H, Xu J, Kromer C, Wolinsky Y, Kruchko C, Barnholtz-Sloan JS. CBTRUS Statistical Report: primary brain and other Central Nervous System tumors diagnosed in the United States in 2009–2013. Neuro Oncol. 2016;18:v1–75.
2. Global Burden of Disease, Cancer C, Kocarnik JM, Compton K, Dean FE, Fu W, Gaw BL, Harvey JD, Henrikson HJ, Lu D, Pennini A, et al. Cancer Incidence, Mortality, Years of Life Lost, Years lived with disability, and disability-adjusted life years for 29 Cancer groups from 2010 to 2019: a systematic analysis for the global burden of Disease Study 2019. JAMA Oncol. 2022;8:420–44.
3. Tan AC, Ashley DM, Lopez GY, Malinzak M, Friedman HS, Khasraw M. Management of glioblastoma: state of the art and future directions. CA Cancer J Clin. 2020;70:299–312.
4. Pavlyukov MS, Yu H, Bastola S, Minata M, Shender VO, Lee Y, Zhang S, Wang J, Komarova S, Wang J, et al. Apoptotic cell-derived extracellular vesicles promote malignancy of Glioblastoma Via Intercellular transfer of splicing factors. Cancer Cell. 2018;34:119–e135110.
5. Di Filippo LD, de Carvalho SG, Duarte JL, Luiz MT, Paes Dutra JA, de Paula GA, Chorilli M, Conde J. A receptor-mediated landscape of druggable and targeted nanomaterials for gliomas. Mater Today Bio. 2023;20:100671.
6. Shi J, Zhao Y, Wang K, Shi X, Wang Y, Huang H, Zhuang Y, Cai T, Wang F, Shao F. Cleavage of GSDMD by inflammatory caspases determines pyroptotic cell death. Nature. 2015;526:660–5.
7. Ding J, Wang K, Liu W, She Y, Sun Q, Shi J, Sun H, Wang DC, Shao F. Pore-forming activity and structural autoinhibition of the gasdermin family. Nature. 2016;535:111–6.
8. Erkes DA, Cai W, Sanchez IM, Purwin TJ, Rogers C, Field CO, Berger AC, Hartsough EJ, Rodeck U, Alnemri ES, Aplin AE. Mutant BRAF and MEK inhibitors regulate the Tumor Immune Microenvironment via Pyroptosis. Cancer Discov. 2020;10:254–69.
9. Wei X, Xie F, Zhou X, Wu Y, Yan H, Liu T, Huang J, Wang F, Zhou F, Zhang L. Role of pyroptosis in inflammation and cancer. Cell Mol Immunol. 2022;19:971–92.
10. Wang Y, Gao W, Shi X, Ding J, Liu W, He H, Wang K, Shao F. Chemotherapy drugs induce pyroptosis through caspase-3 cleavage of a gasdermin. Nature. 2017;547:99–103.
11. Fan JX, Deng RH, Wang H, Liu XH, Wang XN, Qin R, Jin X, Lei TR, Zheng D, Zhou PH, et al. Epigenetics-based Tumor cells pyroptosis for enhancing the Immunological Effect of Chemotherapeutic Nanocarriers. Nano Lett. 2019;19:8049–58.
12. Timbie KF, Afzal U, Date A, Zhang C, Song J, Wilson Miller G, Suk JS, Hanes J, Price RJ. MR image-guided delivery of cisplatin-loaded brain-penetrating nanoparticles to invasive glioma with focused ultrasound. J Control Release. 2017;263:120–31.
13. Niu B, Zhou Y, Liao K, Wen T, Lao S, Quan G, Pan X, Wu C. Pincer movement: reversing cisplatin resistance based on simultaneous glutathione depletion and glutathione S-transferases inhibition by redox-responsive degradable organosilica hybrid nanoparticles. Acta Pharm Sin B. 2022;12:2074–88.
14. Chen J, Pan S, Zhou J, Lin Z, Qu Y, Glab A, Han Y, Richardson JJ, Caruso F. Assembly of Bioactive nanoparticles via Metal-Phenolic Complexation. Adv Mater. 2022;34:e2108624.
15. Xie L, Li J, Wang L, Dai Y. Engineering metal-phenolic networks for enhancing cancer therapy by tumor microenvironment modulation. Wiley Interdiscip Rev Nanomed Nanobiotechnol. 2023;15:e1864.
16. Ren Z, Sun S, Sun R, Cui G, Hong L, Rao B, Li A, Yu Z, Kan Q, Mao Z. A metal-polyphenol-coordinated nanomedicine for synergistic Cascade Cancer Chemotherapy and Chemodynamic Therapy. Adv Mater. 2020;32:e1906024.
17. Xiang J, Li Y, Zhang Y, Wang G, Xu H, Zhou Z, Tang J, Shen Y. Polyphenol-cisplatin complexation forming core-shell nanoparticles with improved tumor accumulation and dual-responsive drug release for enhanced cancer chemotherapy. J Control Release. 2021;330:992–1003.
18. Xu Y, Han X, Li Y, Min H, Zhao X, Zhang Y, Qi Y, Shi J, Qi S, Bao Y, Nie G. Sulforaphane mediates glutathione depletion via Polymeric nanoparticles to restore cisplatin chemosensitivity. ACS Nano. 2019;13:13445–55.

19. Lu Y, Pan Q, Gao W, Pu Y, He B. Reversal of cisplatin chemotherapy resistance by glutathione-resistant copper-based nanomedicine via cuproptosis. J Mater Chem B. 2022;10:6296–306.
20. Wang D, Zhao C, Xu F, Zhang A, Jin M, Zhang K, Liu L, Hua Q, Zhao J, Liu J, et al. Cisplatin-resistant NSCLC cells induced by hypoxia transmit resistance to sensitive cells through exosomal PKM2. Theranostics. 2021;11:2860–75.
21. Zhang L, Du X, Li Q, Qian L, Chen J, Liu C, Yu Q, Gan Z. A Multimodal Therapeutic Nanoplatform overcoming Tumor Hypoxia Heterogeneity for Improved Tumor Chemoradiotherapy. Adv Funct Mater. 2022;32:2204629.
22. Nduom EK, Wei J, Yaghi NK, Huang N, Kong LY, Gabrusiewicz K, Ling X, Zhou S, Ivan C, Chen JQ, et al. PD-L1 expression and prognostic impact in glioblastoma. Neuro Oncol. 2016;18:195–205.
23. Davenne T, Percier P, Larbanoix L, Moser M, Leo O, Meylan E, Goriely S, Gerard P, Wauthoz N, Laurent S, et al. Inhaled dry powder cisplatin increases antitumour response to anti-PD1 in a murine lung cancer model. J Control Release. 2023;353:317–26.
24. Brown MC, Holl EK, Boczkowski D, Dobrikova E, Mosaheb M, Chandramohan V, Bigner DD, Gromeier M, Nair SK. Cancer immunotherapy with recombinant poliovirus induces IFN-dominant activation of dendritic cells and tumor antigen-specific CTLs. Sci Transl Med 2017, 9.
25. Yin T, Fan Q, Hu F, Ma X, Yin Y, Wang B, Kuang L, Hu X, Xu B, Wang Y. Engineered macrophage-membrane-coated nanoparticles with enhanced PD-1 expression induce Immunomodulation for a synergistic and targeted Antiglioblastoma Activity. Nano Lett. 2022;22:6606–14.
26. Dong Y, Zhang J, Wang Y, Zhang Y, Rappaport D, Yang Z, Han M, Liu Y, Fu Z, Zhao X, et al. Intracavitary Spraying of Nanoregulator-Encased Hydrogel modulates cholesterol metabolism of glioma-supportive macrophage for postoperative Glioblastoma Immunotherapy. Adv Mater. 2024;36:e2311109.

Publisher's note